Analytic Damping and Stiffness Analysis for a 4-DOF Electrodynamic Wheel Maglev Vehicle

J. Wright, J. Z. Bird

***Abstract* – This paper analyzes the damping and stiffness terms of a 4-degree of freedom laboratory scale electrodynamic wheel magnetic levitation vehicle. The vehicle creates both suspension and propulsion forces through the simultaneous rotation and translation of the electrodynamic wheels above a conductive non-magnetic plate of finite thickness. The stiffness and damping terms were derived using an analytic 3-D steady-state eddy current model, and are analyzed based on their suitability for a linear state-space model. The implications with respect to static stability are discussed.**

***Index Terms*—damping, electrodynamic wheel, Halbach, levitation, maglev, magnetic, stability, stiffness**

I. Introduction

A significant challenge to the realization of electrodynamic wheel (EDW) magnetic levitation (maglev) vehicles is the current lack of stability and controls analysis on eddy current based systems that utilize conductive plate tracks. Past authors have used lumped parameter circuit based approaches to model the forces created by electrodynamic based maglev system [1-3]. For instance, Ooi [4-7] and Cai [8] used a lumped parameter approach to derive the stiffness and damping terms and then incorporated the terms within a state-space electromechanical maglev model suitable for control. However, lumped parameter based systems are inherently approximate as they cannot account for the skin effect within a conductive plate nor model the complex circulating current density paths within a solid conductor.

Chen *et al.* [9, 10] used an experimental setup to empirically determine the force relationship of a translationally moving coil with respect to velocity and position, this allowed stiffness and damping terms to be empirically determined. Chen termed this approach unsteady-motion theory. Chu *et al.* [11] used a similar type of empirical based approach when studying the dynamics of moving magnets over a conductive plate. However, such an approach can only be used after the maglev system is constructed.

Davis *et al.* [12] and Uranker [13, 14] pioneered the use of using exact analytic eddy current equations to determine the eddy current stiffness and damping terms for a coil translationally moving over a conductive plate. More recently, Paul *et al.* used a second order vector potential (SOVP) formulation to analytically derive the stiffness and damping matrices for an EDW above a conductive plate [15-17]. The EDW has both rotational and translational velocity vectors. A laboratory scale EDW vehicle is shown in Fig. 1 and the vehicles coordinate axes are defined in Fig. 2. The EDW vehicle is physically prevented from moving in the translational, and yaw, θ_y, axis such that $(z,\theta_y) = (0,0)$.

In this paper, the SOVP-calculated stiffness and damping terms are used in a semi-linear 4 degree of freedom (DOF) maglev system, with a focus on stability and linearity. Recognizing which terms are approximately linear within an EDW vehicle's operating region is important, because highly non-linear terms will cause the state-space model to become inaccurate if the vehicle drifts from its desired operating point. The non-linear terms will then need to be re-calculated in real time for the vehicle motion to match the model.

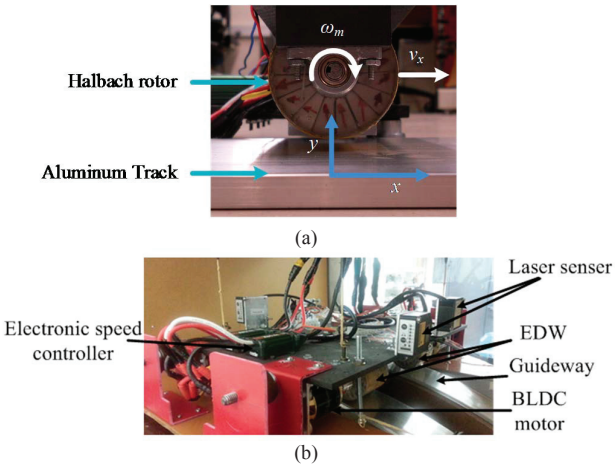

Fig. 1. (a) Single EDW above aluminum conductive plate and (b) vehicle setup consisting of 4 EDW and brushless DC drive motors [18]

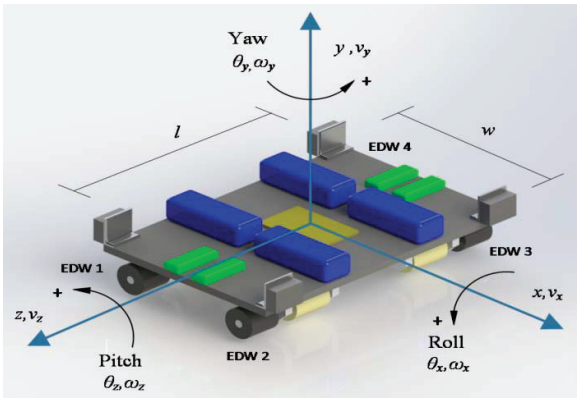

Fig. 2. Mechanical model of prototype EDW maglev vehicle

II. Electrodynamic Wheel Prototype

The rotor and guideway parameters for which the analysis is performed are shown in Table I. The four EDWs have a radius r_o = 26mm and contain P = 2 pole-pairs. The field is created by using a four segment-per-pole Halbach rotor typology. By rotating the EDW over the conductive plate eddy currents are induced in the conductive plate track that create both a lift force and thrust or braking force. A thrust force is created when the rotor circumferential velocity, v_c becomes greater than the translational velocity, v_x. Therefore, a slip speed, s, can be defined as

$$s = v_c - v_x \tag{1}$$

where

$$v_c = r_o \omega_m \tag{2}$$

and ω_m = rotor mechanical angular speed.

If the EDW vehicle is to remain levitated at a desired attitude and location on a conductive track, then it is necessary to control the vertical position, y, translational position (forward and backward), x, roll, θ_x, and pitch, θ_z angle. These variables are defined in Fig. 2. The EDW's are hard-mounted to the vehicle (i.e. not allowed to pivot relative to the vehicle body).

TABLE I
EDW VEHICLE LABORATORY PARAMETERS

Parameter		Value	Unit
Rotor	Outer radius, r_o	26 ± 0.58	mm
	Inner radius, r_i	9.6	mm
	Width of rotor, w_r	52	mm
	Residual flux density, B_{rem}	1.42	T
	relative permeability, μ_r	1.108	-
	Pole-pairs, P	2	-
Guideway	Outer radius, r_g	600 ± 0.73	mm
	Guideway model width, w	140	mm
	Guideway model length, l	140	mm
	Thickness, h	6.3	mm
	Conductivity, σ (Al, 6061-T06)	$2.459\text{x}10^{-7}$	Sm^{-1}

III. 3-D FORCE AND TORQUE EQUATION

If an EDW is rotating with rotational speed, ω_m and is moving with a velocity described by

$$\mathbf{v} = v_x\hat{x} + v_y\hat{y} + v_z\hat{z} \tag{3}$$

then the forces created by the induced eddy currents is [17]

$$\mathbf{F} = \frac{1}{\mu_o}\int_{-l/2}^{l/2}\int_{w/2}^{w/2} B_y^s(x,y_g,z)^*\mathbf{B}^r(x,y_g,z)dxdz \tag{4}$$

Solving for the source field, B_y^s, and the reflected eddy-current field, $\mathbf{B}^r$ the force equation yields

$$\mathbf{F} = wl\,\mathrm{Re}\left\{\sum_{m=-\infty}^{\infty}\sum_{n=-\infty}^{\infty} B_{mn}^s R_{mn}\left[\frac{j\xi_m}{\kappa_{mn}}\hat{x} - \hat{y} + \frac{jk_n}{\kappa_{mn}}\hat{z}\right]\right\} \tag{5}$$

where B_{mn}^s is the source field term and R_{mn} is the reflected eddy current field term for the m^{th} and n^{th} spatial harmonic. The reflected eddy current term is created by the induced currents in the conductive plate and is defined as [17]

$$R_{mn} = \frac{\mu_0\sigma\tau_{mn}}{\xi_m^2 + k_n^2 + \gamma_{mn}^2 + 2\kappa_{mn}\beta_{mn}\coth(\beta_{mn}h)} \tag{6}$$

where

$$\xi_m = 2\pi m/l \tag{7}$$

$$k_n = 2\pi n/w \tag{8}$$

$$\beta_{mn}^2 = \lambda^2 + \gamma_{mn}^2 \tag{9}$$

$$\lambda = -0.5v_y\mu_0\sigma \tag{10}$$

$$\gamma_{mn}^2 = \kappa_{mn}^2 - j\mu_0\sigma(Pw_m + \xi_m v_x + k_n v_z) \tag{11}$$

$$\kappa_{mn}^2 = \xi_m^2 + k_n^2 \tag{12}$$

$$\tau_{mn} = \kappa_{mn}v_y + j(Pw_m + \xi_m v_x + k_n v_z) \tag{13}$$

The terms given in (6) - (13) are defined in Table I. The force equation assumes that the conductive, non-magnetic plate has a model width, w, length, l, and thickness, h, and it is assumed that the plate is sufficiently wide and long that the source and eddy current fields are zero at its length and width edges. The steady-state reflected eddy-current field, $\mathbf{B}^r$, created above the conductive plate is given by [15-17]

$$B^r(x,y,z,t) = -j\sum_{m=-\infty}^{\infty}\sum_{n=-\infty}^{\infty} S_{mn}\frac{R_{mn}}{\kappa_{mn}}\left[\xi_m\hat{x} + j\kappa_{mn}\hat{y} + k_n\hat{z}\right] \times e^{-\kappa_{mn}(y+y_g)}e^{j\xi_m x}e^{jk_n z}e^{-jP\omega_m t} \tag{14}$$

The EDW source field term in (5) is defined by

$$B_{mn}^s = \frac{1}{\mu_0}\left|S_{mn}\right|^2 e^{-2\kappa_{mn}y_g} \tag{15}$$

where S_{mn} is the m^{th} and n^{th} spatial Fourier harmonic source field term and y_g is the air-gap height between the EDW and the conductive plate. The Fourier harmonic source field terms are determined by applying a 2-D spatial Fourier harmonic analysis to the source field. For the EDW, the 3-D steady state source field for a Halbach rotor can be shown to be [15-17]

$$B_y^{so}(x,y,z,t) = \frac{B_r r_o e^{-jP\omega_r t}}{2\pi}\int_0^{2\pi}\int_{-w_0/2}^{w_0/2}\frac{e^{jP\theta_o}}{R^3}(y - y_c - r_o\sin\theta_o)dz_o d\theta_o \tag{16}$$

where

$$B_r = \frac{2B_{res}P(1+\mu_r)(r_i^{P+1} - r_o^{P+1})r_o^{2P}}{(1+P)\left[(1-\mu_r)^2 r_i^{2P} - (1+\mu_r)^2 r_o^{2P}\right]r_o^{P+1}} \tag{17}$$

$$R = \sqrt{(x - x_c - r_o\cos\theta_o)^2 + (y - y_c - r_o\sin\theta_o)^2 + (z - z_c - z_o)^2} \tag{18}$$

The parameters (x_c,y_c,z_c) in (18) defines the center position of the rotor and r_i = inner rotor radius. Utilizing (16) the Fourier harmonic terms can be obtained by evaluating:

$$S_{mn} = \frac{e^{jP\omega_r t}}{lw}\int_{-w/2}^{w/2}\int_{-l/2}^{l/2} B_y^{so}(x,y_g,z,t)e^{-j\xi_m x}e^{-jk_n z}dxdz \tag{19}$$

The Fourier harmonic field at a height y_g can then be expressed in Cartesian form as:

$$B_y^s(x,y_g,z,t) = \sum_{m=-\infty}^{\infty}\sum_{n=-\infty}^{\infty} S_{mn}e^{j\xi_m x}e^{\kappa_{mn}y_g}e^{jk_n z}e^{-jP\omega_m t} \tag{20}$$

where the complex exponential term in (20) accounts for the rotational motion of the source field.

By a similar derivation, the eddy-current torque is [18]

$$T_{em} = wlP\,\mathrm{Im}\left\{\sum_{m=-\infty}^{\infty}\sum_{n=-\infty}^{\infty}\frac{B_{mn}^s R_{mn}}{\kappa_{mn}}\right\} \tag{21}$$

IV. EDDY-CURRENT STIFFNESS AND DAMPING TERMS

In [5], the force and torque term given by (5) and (21) were used to derive 6-DOF stiffness and damping terms. As this laboratory vehicle is suspended above a 1.2m guideway wheel that approximates a flat guideway track it is not desirable to have the vehicle yaw, θ_y, about the y-axis since this could lead to the rotors approaching the edge of the finite width conductive plate guideway. It is also assumed in this analysis that the motion along the axial z-axis, as defined in Fig. 2, is constrained and it is therefore not necessary to model transverse z movement. These constraints result in the eddy current model reducing to a 4-DOF model. The damping and stiffness matrix then reduces to

$$[\mathbf{k}] = \begin{bmatrix} k_{xx} & k_{xy} \\ k_{xy} & k_{yy} \end{bmatrix} = -\begin{bmatrix} \frac{\partial F_x}{\partial x} & \frac{\partial F_x}{\partial y} \\ \frac{\partial F_y}{\partial x} & \frac{\partial F_y}{\partial y} \end{bmatrix} \tag{22}$$

where the diagonal terms are given by

$$k_{xx} = wl\,\mathrm{Re}\left\{\sum_{m=-\infty}^{\infty}\sum_{n=-\infty}^{\infty}\frac{\xi_m^2}{\kappa_{mn}}B_{mn}^s R_{mn}\right\} \tag{23}$$

$$k_{yy} = -wl\,\mathrm{Re}\left\{\sum_{m=-\infty}^{\infty}\sum_{n=-\infty}^{\infty}\kappa_{mn}B_{mn}^s R_{mn}\right\} \tag{24}$$

From the energy equation used to form (4), it can be shown that the diagonal stiffness terms in (22) are equal, so that [17]

$$\frac{\partial F_x}{\partial y} = \frac{\partial F_y}{\partial x} \tag{25}$$

Therefore, the cross diagonal terms in (22) are both equal to

$$k_{xy} = wl\,\mathrm{Re}\left\{\sum_{m=-\infty}^{\infty}\sum_{n=-\infty}^{\infty} j\xi_m B^s_{mn} R_{mn}\right\} \tag{26}$$

Note that the stiffness terms involving rotor angle, θ_m, are cyclic with the electrical frequency of the rotor, $P\omega_m$, and average to zero for the comparatively larger time constants of the vehicle and the torque stiffness and damping terms with respect to x and y, are very small and are therefore neglected.

Using analogous assumptions the damping terms are

$$[\mathbf{d}] = \begin{bmatrix} d_{xx} & d_{xy} \\ d_{xy} & d_{yy} \end{bmatrix} = -\begin{bmatrix} \frac{\partial F_x}{\partial v_x} & \frac{\partial F_x}{\partial v_y} \\ \frac{\partial F_y}{\partial v_x} & \frac{\partial F_y}{\partial v_y} \end{bmatrix} \tag{27}$$

where

$$d_{xx} = lw\,\mathrm{Re}\left\{\sum_{m=-\infty}^{\infty}\sum_{n=-\infty}^{\infty} B^s_{mn}\frac{-j\xi_m}{\kappa_{mn}}\frac{\partial R_{mn}}{\partial v_x}\right\} \tag{28}$$

$$d_{xy} = lw\,\mathrm{Re}\left\{\sum_{m=-\infty}^{\infty}\sum_{n=-\infty}^{\infty} B^s_{mn}\frac{-j\xi_m}{\kappa_{mn}}\frac{\partial R_{mn}}{\partial v_y}\right\} \tag{29}$$

$$d_{xy} = lw\,\mathrm{Re}\left\{\sum_{m=-\infty}^{\infty}\sum_{n=-\infty}^{\infty} B^s_{mn}\frac{\partial R_{mn}}{\partial v_x}\right\} \tag{30}$$

$$d_{yy} = lw\,\mathrm{Re}\left\{\sum_{m=-\infty}^{\infty}\sum_{n=-\infty}^{\infty} B^s_{mn}\frac{\partial R_{mn}}{\partial v_y}\right\} \tag{31}$$

and

$$\frac{\partial R_{mn}}{\partial v_x} = j\xi_m\left[a_{mn} + \tau_{mn}(1+\kappa_{mn}b_{mn})\right] / \, a^2_{mn} \tag{32}$$

$$\frac{\partial R_{mn}}{\partial v_y} = \kappa_{mn}\left[a_{mn} - 0.5 v_y b_{mn}\tau_{mn}\right] / \, a^2_{mn} \tag{33}$$

$$a_{mn} = \left[\kappa^2_{mn} + \gamma^2_{mn} + 2\kappa_{mn}\beta_{mn}\coth(\beta_{mn}h)\right] / \, (\mu_0\sigma) \tag{34}$$

$$b_{mn} = \coth(\beta_{mn}h) / \beta_{mn} - h\,\mathrm{csch}^2(\beta_{mn}h) \tag{35}$$

$$\beta^2_{mn} = \lambda^2 + \gamma^2_{mn} \tag{36}$$

Note that unlike stiffness the diagonal damping terms in (27) are not equal.

V. Analysis of Stiffness Terms

One of the most significant challenges in the realization of an EDW maglev systems is the control of such a non-linear and highly coupled system. Linear control, while computationally efficient, is unsuited for modes of motion that are non-linear and unstable. On the other hand, run-time calculations of stiffness and damping, while significantly faster than other dynamic equations or finite element methods, are still computationally intensive (on the order of tens to hundreds of milliseconds), and need to be minimized for efficient control. The contribution made by this paper is to utilize the analytic damping and stiffness terms defined by (22) and (27) within the framework of a maglev vehicle in order to assess what terms create stability or instability. It should be noted that the derived stiffness and damping terms plotted in this paper are based on a steady-state model. However as the eddy current time constant is much faster than the mechanical time constant it was shown in [19] that the steady-state eddy current force model can be combined with a transient mechanical model to provide valid dynamic results, as long as the steady-state force terms are actively updated when the mechanical parameters change (such as position and velocity). We call negative stiffness and damping terms stabilizing, since they enact a restorative force towards equilibrium.

In the following sections, when analyzing how the damping and stiffness terms are affected by slip, s, v_x, and v_y, it is also beneficial to envision how the vehicle would typically operate. Starting from a standstill, $s = v_x = v_y = 0$, slip increases until the vehicle levitates. Translational speed, v_x, then begins to catch up to slip, until it reaches steady-state, at which point v_x lags behind slip by a consistent amount. Upon braking, slip lags behind v_x by an amount dependent on the amount of braking force desired. This is illustrated in Fig. 3, noting that this is the generalized behavior and the actual regions would vary based on operating conditions.

From Fig. 3, when slip magnitude is significantly larger than the magnitude of v_x and they are both have the same direction, the vehicle operates in the *blue* zone and undergoes acceleration. Steady state or near steady state operation occurs in the *yellow* zone, where slip and v_x operate in the same direction and slip magnitude is only slightly larger than v_x magnitude. As slip slows down, the vehicle will undergo braking, shown by the *green* zone. If the slip direction is reversed, then the vehicle will experience a larger braking force, shown by the *dark pink* zone.

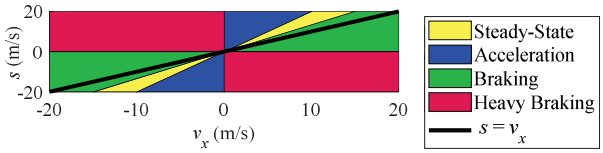

Fig. 3: Approximate vehicle operating regions

A. Translational Thrust Stiffness

Fig. 4 shows the variation of translational force, F_x, with respect to slip, for various values of translational velocity, v_x. Note that a maximum slip and translational velocity magnitude of 20m/s was chosen to keep the Halbach rotors from exceeding their mechanical limitations.

Fig. 5 shows how the translational stiffness in the x-direction, k_{xx}, is affected by slip and v_x when $v_c = 0$ m/s. The near symmetry about the $s = v_x$ line implies that the stiffness is affected similarly by both slip and v_x velocity, as expected from (1). As k_{xx} is always less than zero under these operating conditions, it enacts a force towards equilibrium and is therefore a stabilizing influence in the x-direction. When either v_x or slip increases in magnitude, the stabilizing force becomes greater. Fig. 6 better shows the behavior when the vertical speed and circumferential speed are held at $(v_y, v_c) = (0,10)$ m/s. A rotor circumferential speed of $v_c = 10$ m/s equates to $\omega_m = 3691$ rev/min. This value was selected as it is

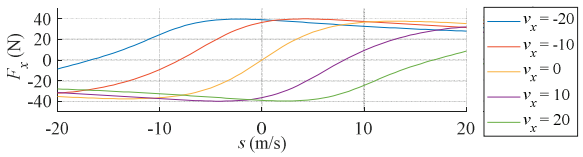

Fig. 4. F_x vs. slip for various values of translational velocity, v_x

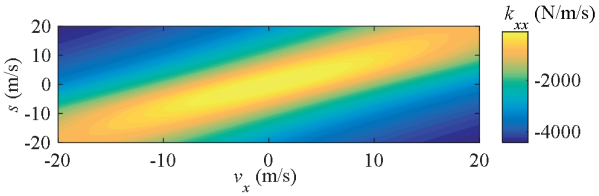

Fig. 5. Contour plot of k_{xx} vs. slip vs. v_x, ($v_y = 0$)

a sufficient rotational speed to levitate the prototype vehicle. A minimum stiffness is achieved when the x velocity is offset by the rotor velocity such that

$$v_x = r_o \omega_r \tag{37}$$

In steady-state operation, k_{xx} is less stabilizing, and becomes more stabilizing as the vehicle accelerates and decelerates significantly. Light braking that moves the system towards equation (37) can minimize the stabilization.

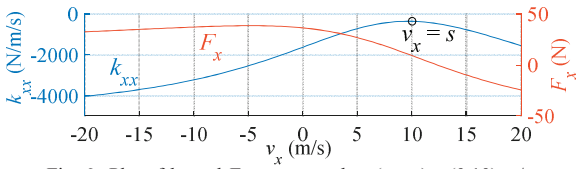

Fig. 6. Plot of k_{xx} and F_x versus v_x when $(v_y, v_c) = (0,10)$ m/s.

In order to evaluate how v_y affects k_{xx}, it can first be observed how the force is affected by a range of heave values, as shown in Fig. 7. Note that any non-zero heave is considered transient, and is expected to be small, so the v_y terms only range from ±5 m/s.

The contour plot in Fig. 8 shows how k_{xx} changes as slip and v_y vary, while $v_x = 0$. While k_{xx} is negative and therefore stabilizing for a majority of the operating region, k_{xx} becomes positive and therefore destabilizing when the vertical velocity is strongly positive and the slip is small. While this must be accounted for when considering transient behavior, during cruise, the vehicle would have significant slip and very little vertical velocity.

It can also be noted that increasing slip magnitude is a stabilizing action on k_{xx} with respect to v_y, since increasing the slip magnitude drives the stiffness down. Fig. 9 shows that when the rotor speed is held constant at $(v_x, v_c) = (0,10)$ m/s, k_{xx} increases nearly linearly with v_y. This bolsters the argument for linearizing this dynamic for control purposes. Also note that at this reasonable rotor speed, k_{xx} is always negative and therefore stabilizing.

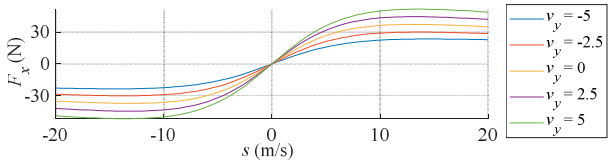

Fig. 7. Thrust force, F_x, versus slip for various values of v_y ($v_x = 0$)

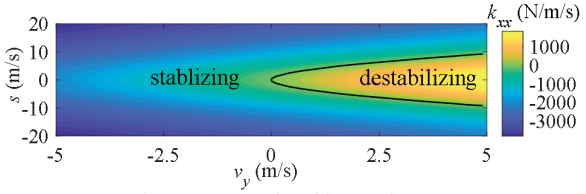

Fig. 8. Contour plot of k_{xx} vs. slip vs. v_y
(note $v_x = 0$, so slip is $s = \omega_m r_o$)

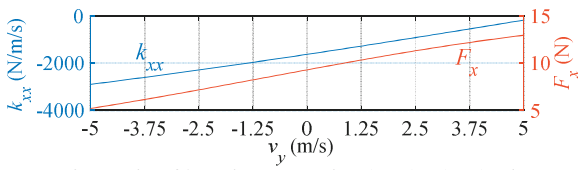

Fig. 9. Plot of k_{xx} and F_x, vs. v_y when $(v_x, v_c) = (0,10)$ m/s

B. *Translational Heave Stiffness*

The definition of the translational heave stiffness, k_{xy}, is given by (26) it is the partial derivative of the thrust force with respect to the vertical position change.

Note that due to symmetry of the stiffness matrix defined in equation (22), k_{xy}, can also be thought of as the partial derivative of the lift force with respect to change in translational position. Therefore, due to this off-diagonal equivalence in (22), the vertical force will be affected by δx the same way that translational force is affected by δy.

Fig. 10 shows the relationship of k_{xy} with slip and v_x. The near symmetrical behavior about $s = v_x$ is expected from equation (1). Note that despite the nonlinear behavior, there exists a general trend of a positive, destabilizing stiffness for larger slip and translational velocities, and a negative, stabilizing stiffness for smaller slip and translational velocities. The line $s = v_x$ is the cutoff between stabilizing and destabilizing k_{xy} contribution. From Fig. 3, we can see that this dynamic would be strongly stable during acceleration, weakly stable during steady-state operation, and less stable as more braking force is applied. Note that stability while braking is only possible when only a small brake force is applied as to not cross the $s = v_x$ threshold.

Fig. 11 shows how k_{xy} changes as v_x changes while $(v_y, v_c) = (0,10)$ m/s. The non-linear, non-quadratic behavior can have an adverse impact on the application of control if we chose to use a linear system representation, necessitating updating the model during run-time to reflect the actual k_{xy} term. Large forward translational speeds (an expected operating condition) lead to instability.

The contour plot in Fig. 12 shows how k_{xy} varies with slip and v_y. Slices of k_{xy} with respect to slip show that k_{xy} becomes more stabilizing with increased slip and slices of k_{xy} with respect to v_y show that k_{xy} is more stabilizing with increased v_y when slip is positive and more destabilizing with increased v_y when slip is negative. From (26) we can also infer the same stabilizing/destabilizing action in the x-axis. A slice of k_{xy} versus v_y in Fig. 11 shows a strong linearity around an operating point with constant rotor velocity. This term therefore lends itself well to linear modeling in this mode.

Observing both Fig. 10 and Fig. 12, a possible detrimental synergistic effect can be noticed. If the system is operating in an unstable braking region, then the braking force will be increased, leading to a larger change in x. This larger change in x, from (26), will lead to larger changes in F_y and therefore y, which, because of (25), will lead to larger changes in F_x and therefore x, thus indicating a positive feedback loop.

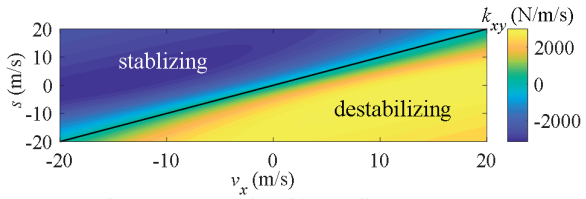

Fig. 10. Contour plot of k_{xy} vs. slip vs. v_x, ($v_y = 0$)

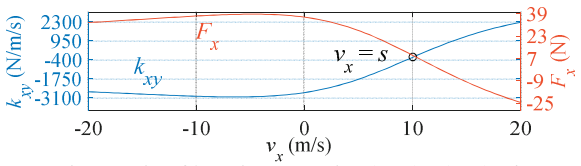

Fig. 11. Plot of k_{xy} and F_x vs. v_x when $(v_y, v_c) = (0,10)$ m/s

C. *Vertical Heave Stiffness*

The vertical heave stiffness, k_{yy}, is defined by (24) and is the partial derivative of F_y with respect to vertical position, y. The vertical lift force, F_y, is always positive when $v_y = 0$ and roughly tends to increase when the quantity s - v_x increases, as shown in Fig. 14.

The contour plot in Fig. 15 shows the relationship of k_{yy} with slip and v_x. Again we obtain near symmetry about $s = v_x$. The negative values suggest k_{yy} with respect to slip and v_x is always stabilizing under these expected operating conditions. Additionally, the magnitude gets larger for larger slip and v_x values, further applying restorative forces. The magnitude of k_{yy} at extreme slip and translational velocities is also larger than other stiffness terms, so k_{yy} has a very pronounced open loop stabilizing effect. The negative k_{yy} value is why past researchers have stated that electrodynamic levitation is stable [8]. Fig. 16 shows a slice of k_{yy} vs. v_x, showing a nonlinear characteristic when $(v_y, v_c) = (0,10)$ m/s. Note that for mild braking in the vicinity of $s = v_x$, there is a reduction in the stabilizing force, but during more pronounced transient operation (accelerating or braking), k_{yy} increases.

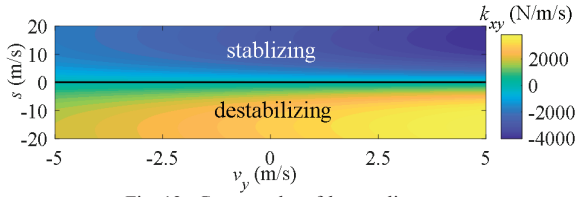

Fig. 12. Contour plot of k_{xy} vs. slip vs. v_y (note $v_x = 0$, so slip is analogous to ω_m)

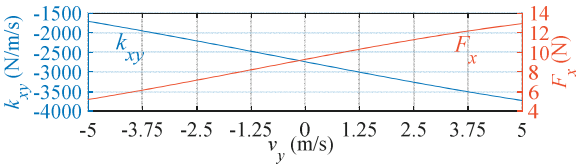

Fig. 13. Plot of k_{xy} and F_x vs. v_y when $(v_x, v_c) = (0,10)$ m/s

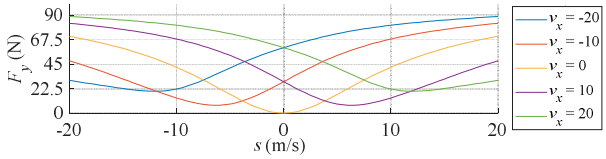

Fig. 14. F_y vs. slip for various values of v_x

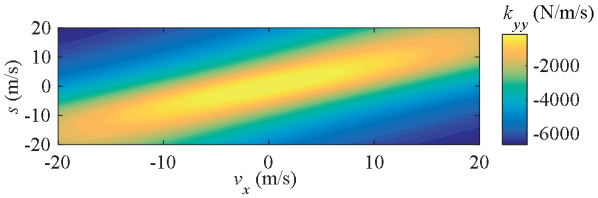

Fig. 15. Contour plot of k_{yy} vs. slip vs. v_x ($v_y = 0$)

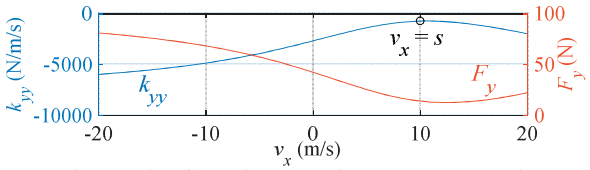

Fig. 16. Plot of k_{yy} and F_x vs. v_x when $(v_y, v_c) = (0,10)$ m/s

The variation of vertical force with respect to vertical velocity is shown in Fig. 17. The contour plot in Fig. 18 shows how k_{yy} is affected by slip and v_y. The k_{yy} and v_y terms are positively correlated, implying that increasing v_y reduces stabilizing action. More stability is observed as the slip magnitude increases. This is a fortunate dynamic, since one would expect a significant slip in order to maintain an airgap and provide thrust. Fig. 19 shows this strong linearity when rotational velocity is held such that $(v_x, v_c) = (0,10)$ m/s. This can be exploited to simplify run-time re-calculations of k_{yy} in a state-space system.

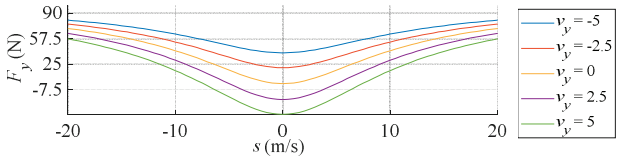

Fig. 17. F_y vs. slip for various values of v_y

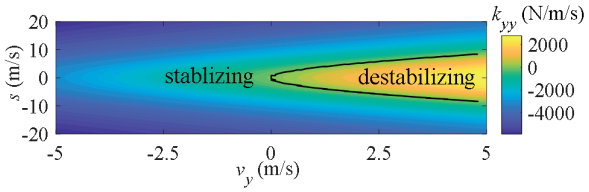

Fig. 18. Contour of k_{yy} vs. slip vs. v_y (note $v_x = 0$, so slip is analogous to ω_m)

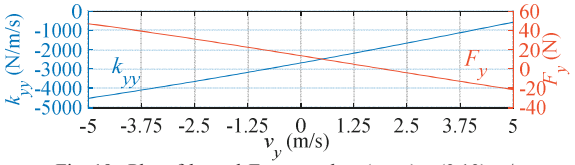

Fig. 19. Plot of k_{yy} and F_x vs. v_y when $(v_x, v_c) = (0,10)$ m/s

VI. Analysis of Damping Terms

A. *Thrust Translational Damping*

The thrust translational damping, d_{xx}, is defined in (28) as the partial derivative of F_x with respect to v_x. Fig. 20 shows the how d_{xx} varies with slip and v_x. Stabilizing damping is observed near $s = v_x$. The damping increases nonlinearly as the system moves away from this line until plateauing near zero for large slip and v_x values. Fig. 21 shows the behavior of d_{xx} as v_x varies and $(v_y, v_c) = (0,10)$ m/s. When the rotor's surface velocity matches the x velocity, the damping is minimized to produce more stable dynamics. The non-linear behavior means a more compute-intensive algorithm is required for re-calculating d_{xx} during run-time, rather than a linear interpolation.

Steady-state cruising and mild to moderate braking will keep the EDW in the stable region. Heavy acceleration and emergency braking will push d_{xx} towards instability.

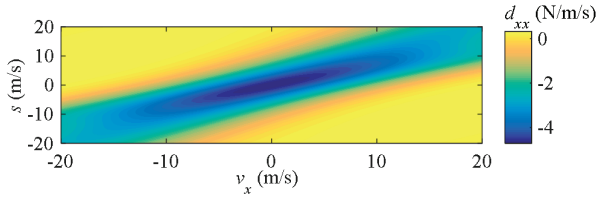

Fig. 20. Contour plot of d_{xx} vs. slip vs. v_x, ($v_y = 0$)

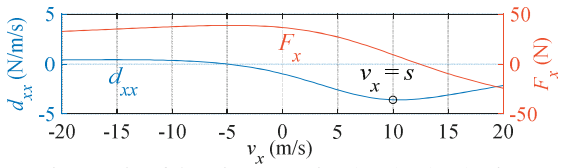

Fig. 21. Plot of d_{xx} and F_x vs. v_x when $(v_y, v_c) = (0,10)$ m/s

The contour plot in Fig. 22 shows the relationship of d_{xx} with respect to slip and v_y. While slices with respect to slip are non-linear, slices with respect to v_y are only weakly non-linear and for control purposes may be approximated as linear. Reduced slip magnitude and larger vertical velocities affect the stabilization on d_{xx}. During operation one would expect slip to be moderately large, which would lead to a near zero contribution on the x-axis dynamics from d_{xx}. Fig. 23 confirms that while d_{xx} vs. v_y is not exactly linear, it could be approximated as linear within a subset of the operating region.

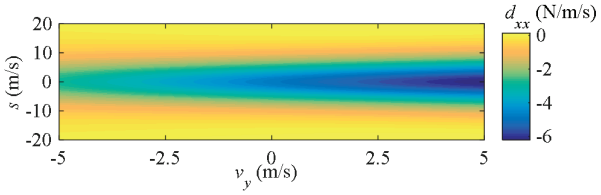

Fig. 22. Contour plot of d_{xx} vs. slip vs. v_y (note $v_x = 0$, so slip is analogous to ω_m)

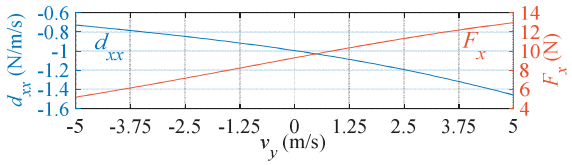

Fig. 23. Plots of d_{xx} and F_x vs. v_y when $(v_x, v_c) = (0,10)$ m/s

B. *Translational Heave Damping*

The thrust translational damping, d_{xy}, is defined as the partial derivative of F_x with respect to v_y. Fig. 24 shows that d_{xy} varies with v_x and slip non-linearly. The largest and smallest values of d_{xy} lie in the heavy braking operating region. Note that for negative values of the quantity v_x - s, the translational heave damping is stabilizing, while for positive values of $v_x - s$, it is destabilizing. The non-linearity complicates the linear modeling and control of the system, and will require updating the d_{xy} term using the analytic model during run-time to achieve high accuracy. A near-zero damping is observed when $s = v_x$. Fig. 25 shows one slice of d_{xy} vs. v_x when $(v_y, v_c) = (0,10)$ m/s, again showing nonlinearity and the fact that faster translational velocity leads to instability in d_{xy}.

As the vehicle accelerates from a standstill, the damping is pushed into the negative region. As v_x increases up to steady-state, the damping magnitude is decreased, but remains negative. Beyond mild braking (s - $v_x < 0$) the damping becomes positive and destabilizing.

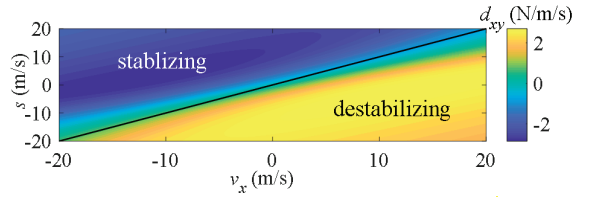

Fig. 24. Contour plot of d_{xy} vs. slip vs. v_x, $(v_y = 0)$

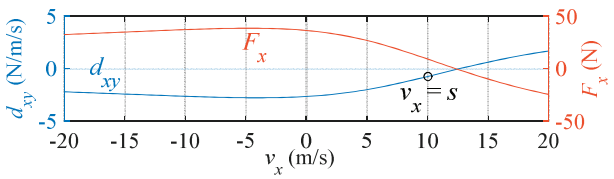

Fig. 25. Plot of d_{xy} and F_x vs. v_x when $(v_y, v_c) = (0,10)$ m/s

The contour plot in Fig. 26 show how d_{xy} varies with slip and v_y. The heave, v_y, does not have a large effect on d_{xy}. This is convenient for an accurate linearization around an operating point in this region. The nonlinear behavior with respect to slip shows that d_{xy} is negative in the expected run-time scenario where slip is positive, and therefore stabilizing when $v_x = 0$. Fig. 27 shows the quadratic shape of d_{xy} with respect to v_y. To reduce compute time, d_{xy} variation in v_y could be approximated by a quadratic function during run-time. Note the stabilizing effect of d_{xy} when $(v_y, v_c) = (0,10)$ m/s, although the stabilization becomes smaller as the magnitude of v_y increases.

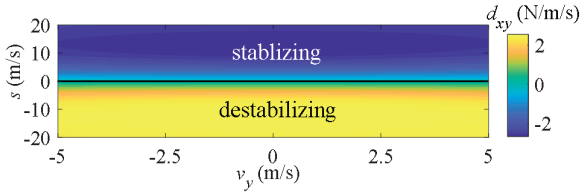

Fig. 26. Contour plot of d_{xy} vs. slip vs. v_y (note $v_x = 0$, so slip is analogous to ω_m)

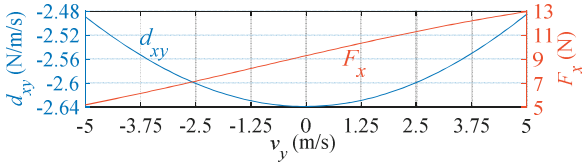

Fig. 27. Plot of d_{xy} and F_x vs. slip vs. v_y when $(v_x, v_c) = (0,10)$ m/s

VII. Discussion

The stability of the selected damping and stiffness terms in relation to v_x when $(s, v_y) = (0,0)$ is summarized in Table II. Note that k_{xy} and d_{xy} are unstable when v_x is positive, and d_{xx} becomes unstable if the magnitude of v_x becomes large enough. Another positive feedback loop exists between k_{xx} and d_{xy} for positive v_x values, since k_{xx} can exert more effect on F_x (and therefore v_x) with larger δy, and d_{xy} becomes increasingly unstable with larger v_x. From a control perspective, Table II shows that k_{xy} and d_{xy} should be recalculated at run-time when v_x changes.

The stability in relation to v_y when $(s, v_x) = (0,0)$ is shown in Table III, which indicates that k_{xx} and k_{yy} are unstable when v_y is positive, and that v_y does not have a strong influence on k_{xy} and d_{xy} at this operating point.

TABLE II
STABILITY OF DAMPING AND STIFFNESS TERMS WHEN $(s, v_y) = (0,0)$ AND v_x VARIES

Term	v_x (m/s) -20	-10	0	10	20	Legend
k_{xx}						UNSTABLE
k_{xy}						
k_{yy}						STABLE
d_{xx}						
d_{xy}						

TABLE III
STABILITY OF DAMPING AND STIFFNESS TERMS WHEN $(s, v_x) = (0,0)$, AND v_y VARIES

Term	v_y (m/s) -5	-2.5	0	2.5	5	Legend
k_{xx}						UNSTABLE
k_{xy}						
k_{yy}						STABLE
d_{xx}						
d_{xy}						

Finally, the stability in relation to s when $(v_x, v_y) = (0,0)$ is shown in Table IV. In this case, k_{xy} and d_{xy} are unstable

when s is negative and d_{xx} becomes weakly unstable when the magnitude of s becomes large. The synergistic effect (positive feedback loop) when k_{xy} and d_{xy} are both positive is also present with the slip dynamic.

TABLE IV
STABILITY OF DAMPING AND STIFFNESS TERMS WHEN (v_y,v_x) =(0,0) AND s VARIES

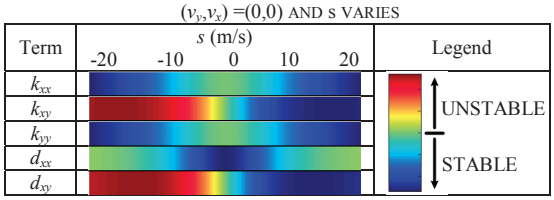

From a control perspective, these tables show that k_{xy} and d_{xy} should be recalculated at run-time when v_x or s changes, while k_{xx} and k_{yy} should be recalculated when v_y changes. Other terms should be recalculated periodically as cpu time permits to keep the estimated system as accurate as possible.

VIII. Conclusion

In this paper, an exact 3-D eddy current based stiffness and damping model has been used to study the static stability of a 4-DOF EDW maglev system. Although many of the terms are highly nonlinear, one can make general notes about the stability contribution of these terms in the operating regions and one can determine which terms can be treated as linear and which must be recalculated during run-time.

IX. Acknowledgment

The authors gratefully acknowledge the contributions of N. Paudel, W. Bomela and S. Paul for their work on electrodynamic suspension maglev systems.

X. References

[1] K. R. Davey, "Electrodynamic maglev coil design and analysis," *IEEE Transactions on Magnetics*, vol. 33, no. 5, pp. 4227-4229, Sept. 1997.

[2] J. Boeij, M. Steinbuch, and H. Gutierrez, "Real-time control of the 3-DOF Sled dynamics of a null-flux Maglev system with a passive sled," presented at the IEEE International Symposium on Industrial Electronics, Jul. , 2006.

[3] N. Kim and L. Ge, "Dynamic modeling of electromagnetic suspension system," *Journal of Vibration and Control*, vol. 19, no. 5, pp. 729-741, 2012.

[4] B. T. Ooi, "Electromechanical stiffness and damping coefficients in the repulsive magnetic levitation system," *IEEE Transactions on Power Apparatus and Systems*, vol. 95, no. 3, pp. 936-943, May/June 1976.

[5] B. T. Ooi, "A dynamic circuit theory of the repulsive magnetic levitation system," *IEEE Transactions on Power Apparatus and Systems*, vol. 96, no. 4, pp. 1094-1100, July 1977.

[6] B. T. Ooi and M. Ivanes, "Stiffness and damping matrices in free-body translational electromechanics," *Elect. Mach. Power Sys.*, vol. 5, no. 1, pp. 15-23, 1980.

[7] B. T. Ooi and O. P. Jain, "Moments and force densities of the electrodynamic levitation system," *IEEE Transactions on Magnetics*, vol. 15, no. 3, pp. 1102-1108, May 1979.

[8] Y. Cai, D. M. Rote, T. M. Mulcahy, Z. Wang, S. S. Chen, and S. Zhu, "Dynamic Stability Experiment of Maglev Systems," Argonne National Laboratory Center for Transportation Research, Argonne, IL, ANL-95/10, 1995.

[9] S. S. Chen, Zhu, S., and Cai, Y, "On the Unsteady-Motion Theory of Magnetic Forces for Maglev," Argonne National Laboratory, Technical Report1993.

[10] S. S. Chen, S. Zhu, and Y. Cai, "On unsteady-motion theory of magnetic forces for maglev systems," *Jour. Sound Vib.*, vol. 188, no. 4, pp. 529-543, 1995.

[11] D. Chu and F. C. Moon, "Dynamic instabilities in magnetically levitated models," *Journal of Applied Physics*, vol. 54, no. 3, pp. 1619-1625, March 1983.

[12] L. C. Davis and D. F. Wilkie, "Analysis of motion of magnetic levitation systems: implications for high-speed vehicles," *Jour. of Appl. Phy.*, vol. 42, no. 12, pp. 4779-4793, Nov. 1971.

[13] L. Urankar, "Intrinsic damping in basic magnetic levitation systems with a continous sheet track," *Siemens Forschungs -und Entwicklungsberichte*, vol. 5, no. 2, pp. 110-119, 1976.

[14] l. Urankar, "Electrodynamics of finite width guideway maglev systems in an integral equation formulation," *Siemens Forschung Entwicklungsberichte*, vol. 8, no. pp. 204-208, 1979.

[15] S. Paul, "Three-dimensional steady state and transient eddy current modeling," Ph.D. Thesis, Elect. Comp. Eng., Univ. N.C. at Charlotte, Charlotte,NC, 2014.

[16] S. Paul, W. Bomela, N. Paudel, and J. Z. Bird, "3-D Eddy Current Torque Modeling," *IEEE Trans. Mag.*, vol. 50, no. 2, pp. 905-908, 2014.

[17] S. Paul, J. Wright, and J. Z. Bird, "3-D Steady-State Eddy-Current Damping and Stiffness Terms for a Finite Thickness Conductive Plate," *IEEE Trans Magn.*, vol. 50, no. 11, pp. 1-4, 2014.

[18] S. Paul, W. Bomela, N. Paudel, and J. Z. Bird, "3-D eddy current torque modeling," *IEEE Trans. Magn.*, vol. 50, no. 2, p. 7022404, Feb. 2014.

[19] N. Paudel, S. Paul, and J. Bird, "Dynamic Electromechanical Eddy Current Force Modeling," *COMPEL: Intern. Jour. Comp. Math. Elect. Elec. Eng.*, vol. 33 no. 6, pp. 2101 - 2120, 2014.

XI. Biographies

Jason Wright was born in Montréal, Canada on Nov. 14, 1988. Following Montréal, he spent years growing up in Toronto, Canada, Cleveland, Ohio, and finally Charlotte, North Carolina, where he currently resides with wife, Hannah.

He graduated from The University of North Carolina at Chapel Hill with a degree in Applied Sciences – Biomedical Engineering. He continued his studies with a Master's Degree in Electrical Engineering from The University of North Carolina at Charlotte, where he is currently a doctoral candidate.

His research interests include magnetics, system modeling, and controls.

Jonathan Z. Bird (M'02) received the B.S. degree from the University of Auckland, New Zealand, in 2000 and the M.S. and Ph.D. degrees from the University of Wisconsin–Madison, Madison, WI, USA, in 2004 and 2006, respectively. From 2006 to 2008, he was a Senior Design Engineer with the General Motors Advanced Technology Center, Torrance, CA, USA. From 2009 to 2015, he was an Assistant and then Associate Professor at the University of North Carolina at Charlotte, Charlotte, NC, USA. Dr. Bird is currently an Associate Professor at Portland State University, Portland, OR, USA. His research interests include electric machine design, electromagnetics, and control.